# Counter-flow Ionic Winds for Localized Hot Spot Cooling

Sajanish Balagopal
David B. Go[#]
Department of Aerospace and Mechanical Engineering
University of Notre Dame
Notre Dame, IN 46556
[#]Email: dgo@nd.edu

*Abstract*—**In this paper, heat transfer enhancement of a heated plate experiencing low velocity forced convection is considered. A wire-to-rod corona electrode configuration was used to generate a counter-flow ionic wind so as to direct the bulk gas flow in such a manner as to induce hot spot cooling. Particle image velocimetry (PIV) studies were conducted to profile the interaction between the bulk flow and counter-flow ionic wind and show how the hydrodynamic interactions result in a downward flow toward the heated surface and characteristic vorticial structures. This impingement-like effect enhanced the convection cooling of the heated plate, reducing the temperature by as much as 5 K. In these PIV experiments, seeding particles were used to obtain the fluid flow profile. As a corona discharge creates a charged environment, seeding particles may get charged, and this may result in deviation from fluid flow due to Coulombic forces. To ensure the fidelity of the PIV results in these experiments, a simplified particle tracking analysis was conducted, solving the modified Basset-Boussinesq-Oseen (BBO) equation for particle motion and including charging and electric field effects to simulate the effects of the corona discharge. The results obtained from these simulations were used to affirm the validity of the PIV results.**

## I. Introduction

Due to increasing performance and portability requirements of electronic devices, there is an ongoing need for heat transfer enhancement to air cool the processors in devices, associated components, finned heat sinks, and the surface of the device in contact with the user. A corona discharge occurs when a high potential difference is applied between two electrodes, one of them with high curvature geometry. During this discharge, the ions generated near the highly curved electrode move towards the oppositely charged electrode and transfer momentum to the neutral air molecules on the way. This can introduce a low velocity bulk gas motion known as an ionic wind, which can thus be used to generate or enhance forced convection heat transfer by appropriate selection of the electrode geometry and location. Because an ionic wind can modulate and distort a pre-existing bulk flow, a controlled convection enhancement can be achieved by varying the magnitude and direction of the electric field. The advantages of this method include direct conversion of electric energy to kinetic energy without any moving parts, low power consumption, and little to no acoustic signature. The applications of corona discharges and ionic winds have been studied in surface cooling [1-5], drag reduction [6-11] and flame kinetics [12]. Marco and Velkoff [1] studied the use of this technique as early as 1963. Even though there are charged species present in the fluid medium, the ratio of

free charges to that of neutral molecules is around $10^{-10}$ [2]. Hence the changes in heat transfer rate can be explained on the basis of fluid mechanics rather than due to changes in physical properties like thermal conductivity and viscosity [3]. Velkoff and Godfrey [2] noted that the effect of ionic wind (corona discharge) on heat transfer is small or non-existent at higher bulk fluid velocities, as the electric body force is insufficient to overcome the inertia of the bulk flow. They had used an array of elevated wires parallel to the flow as corona electrodes and the heated plate as the collecting electrode, noting that the non-dimensionalised temperature profiles with the corona at lower bulk fluid velocities resembled that at higher bulk velocities with no corona current. Earlier works by Go et al. [4-5] used ionic winds to promote hot spot cooling in external flow. The ionic wind was used in the presence of an external flat plate flow to modulate the boundary layer where heat transfer enhancement was desired. The local heat transfer coefficient was observed to be enhanced by up to 200% over that obtained from the bulk flow alone.

The heat transfer enhancement using ionic wind can be adjusted by appropriate selection of electrode geometry, placement, electrode spacing, and discharge voltage. For example, Molki et al. [13] studied the application of ionic wind for heat transfer enhancement in the developing region of a circular tube. The co-axial electrode arrangement where the corona electrode was along the axis of the tube generated a radial ionic wind normal to the flow, generating local and average heat transfer coefficient enhancement of 14-23% and 6-8% respectively. A literature review of the applications of ionic wind in heat transfer enhancement is also noted in his paper. Similarly, works by Allen et al. [14], Ohadi et al. [15], and Laohalertdecha et al. [16] all review electrohydrodynamic enhancement of heat transfer. Many of the recent works on application of ionic wind heat transfer enhancement have concentrated on use of co-flow ionic wind. In co-flow ionic wind, the ionic wind direction is same as that of the bulk flow direction. In the case of an electrode combination flush mounted with the wall, the ionic wind has been used to accelerate the flow in the boundary layer, effectively thinning it to increase advection or delay separation, reducing drag [4,5,9-11]. A counter-flow ionic wind (Fig. 1) can be used to effectively divert an otherwise parallel flow towards the boundaries. Compared to a co-flow situation, a counter electrode positioned appropriately will be able to give hot spot cooling to both the horizontal boundary walls by diverting the flow.

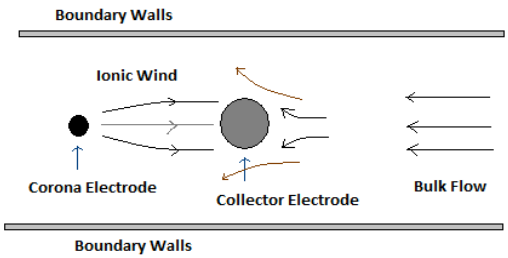


Fig. 1. Counter-flow ionic wind using a corona generated by a wire-cylinder electrode combination (Not to scale).

In this paper, counter-flow ionic wind heat transfer enhancement of a heated plate experiencing low velocity forced convection is considered. A positive polarity, wire-to-cylinder electrode configuration was used to generate a counter-flow ionic wind in order

to induce hot spot cooling. Particle image velocimetry (PIV) measurements revealed the fluid interactions that result in cooling of the heated plate. To ensure the validity of the PIV results, a simulation was conducted to investigate if the seeding particles are adversely affected by charging in the discharge region.

## II. EXPERIMENTAL METHODS

### *A. Experimental setup*

A schematic and photograph of the corona discharge experiment are shown in Fig. 2. A miniature wind tunnel was constructed, and consisted of a flow straightener at the tunnel entrance and a fan operating in suction mode at the tunnel exit, which pulled the air through the straightener into the tunnel creating a bulk flow. The whole structure was made from electrically insulating plastic, and the length, width and height of the tunnel were 179 mm, 51 mm, and 19 mm respectively. For the experiment, the fan voltage (0-25 V E3631A, Agilent) was adjusted such that it provided two bulk flow speeds of approximately 1.0 m/s and 1.6 m/s. For these bulk flow speeds, the Reynolds numbers based on the hydraulic diameter were $Re_{Dh}$ = 1765 and 2825, respectively, which is in the transition region. However, direct visualization of the flow suggested that the flow was laminar for both cases. The entrance length for both velocities was greater than a meter, such that the flow was always in the developing region. As such, the corona electrodes were essentially in a free stream, laminar flow. (The Reynolds numbers based on the length of the duct was $Re_L$ = 11415 and 18265, respectively.)

The electrodes consisted of a 50 μm tungsten wire as the corona electrode and a 1.57 mm outer diameter copper cylinder as the collecting electrode. In order to generate a counter-flow ionic wind, the electrodes were placed with the corona wire downstream of the collecting electrode such that the discharge was in a direction opposite of the bulk flow. The electrodes were separated by a spacing of 4.7 mm (electrode edge-to-edge) as shown in Fig. 3. The power for the corona electrode was provided by a 0-10 kV direct current (DC) high voltage power supply (Bertran Series 225). A positive DC voltage ranging from 6.5-7.3 kV was applied on the corona wire electrode, and the collecting electrode was maintained at ground. The corona current was measured with a picoammeter at the grounded electrode (Keithley 6485).

The PIV measurements were conducted using a FlowMaster Planar PIV system (LaVision Inc.). A 532 nm Nd:YAG laser with a pulse energy of 30 mJ (Solo II-30, New Wave Research) was used to provide light during exposure, and images were recorded using an Imager ProX 2M camera. For single frame images, a frequency rate of 30 fps was possible, and for PIV experiments, double frame/double exposure images were taken with the camera frequency rate at 14.7 Hz. The timing between the two images (for each set of double frame image) was varied from 28-32 μs, depending upon the bulk velocity used. The wind tunnel was kept in an optically transparent box that was filled with seeding particles provided by incense sticks, and the seeding density was controlled by the burning time. Cross correlation analysis on the images was conducted using Davis 7 software with variable windows size (final size is 32 by 32 pixels) and 50% overlap.

For heat transfer measurements, a Teflon sheet, 1 mm in thickness, was placed in a counter-sunk recess, flush with the surface of the bottom horizontal wall of the tunnel as shown in Fig. 2. It extended 31 mm upstream and 46 mm downstream of the collecting

electrode. The Teflon sheet was placed such that any flow modification effected by the ionic wind will occur primarily within the length of the Teflon sheet, thus capturing the heat transfer enhancement of the ionic wind. K-type thermocouples (HSTC-TT-K, Omega Engineering) were used to measure the local temperature of the Teflon sheet and were placed just below the surface at four locations as shown in Fig. 3. The thermocouples were read using a K-type thermocouple thermometer (Omega 450 AKT). Two 2.5 cm by 5 cm film heaters (KHLV series, Omega Engineering) were placed at the bottom of the recess, and a thermally conductive putty (TIM-putty, Timtronics) was used to fill any space between the thermocouple, heater, and Teflon sheet and to ensure good thermal contact. The Teflon sheet was painted with Krylon ultra flat black spray 1602 of known emissivity on the side exposed to wind tunnel flow [17], in order to accurately calculate radiation. The the two heaters were powered by a variable transformer power supply (Variac series, ISE Inc.) and operated so that a constant total heat of 2.3 W was delivered to the Teflon sheet.

### *B. Measurements*

PIV experiments were initially run without ionic wind (no corona discharge) to determine the effect of the physical presence of the electrodes alone on the fluid flow. Following this, PIV was conducted over a series of combinations of corona currents (20 μA and 40 μA) and bulk fluid velocities (1.0 m/s and 1.6 m/s). Fan speeds were initially run much higher than these velocities to facilitate better seeding homogeneity in the tunnel, and then reduced to their experimental values. Thirty images were taken for all experiment runs and the results presented herein were time-averaged across all the images.

The heat transfer experiments were conducted independently of the PIV studies to avoid precipitating the seeding particles. The heater and fan were set at their required settings for the heater power and experimental bulk flow velocity, respectively. After the temperatures measured by the thermocouples reached steady state values, a corona discharge was activated. The temperatures were then measured until they reached steady state values.

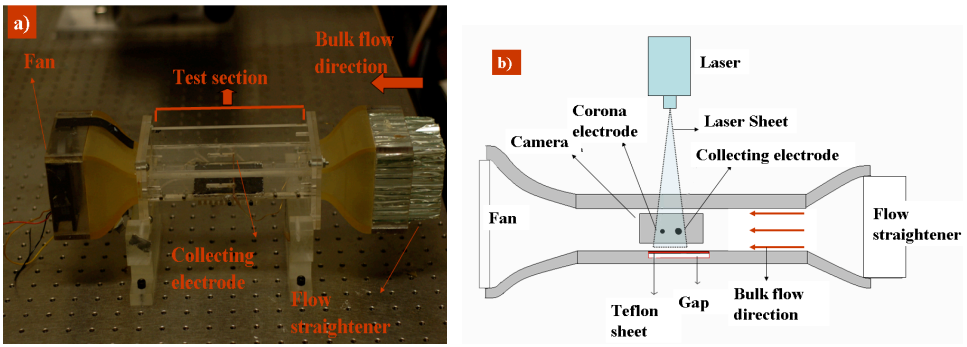


Fig. 2 (a) Photograph and (b) schematic (side view) showing the wind tunnel and electrode positions. The heaters were placed in the gap shown under the Teflon sheet. For heat transfer measurements, thermocouples were placed just under the Teflon sheet, but above the heaters. The PIV laser illuminated the flow from the top, aligned with the midline of the tunnel, and the PIV camera recorded images normal to laser sheet (from the perspective of the reader).

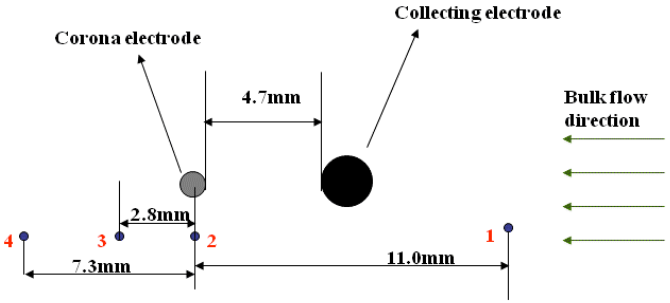


Fig. 3. Schematic showing electrode-electrode separation distance and thermocouple positions. Thermocouple locations are indicated by dots numbered 1-4.

## III. EXPERIMENTAL RESULTS

### *A. PIV Measurements*

For the PIV measurements without an active ionic wind, the effects of the electrodes on the flow were found to be limited to a small region near the tunnel centerline (the electrode plane). Fluid flow near the walls was unaffected by the presence of electrodes. Vortex shedding was observed through smoke visualization (Fig. 4), as anticipated, but notably, it was present only when the ionic wind was not activated. The bulk fluid velocity was determined based on these measurements.

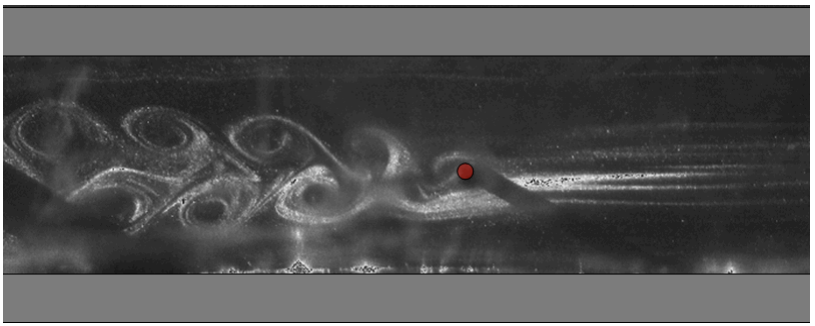

Fig. 4. Vortex shedding observed in the wind tunnel in the absence of ionic wind. Red dot indicates the collecting electrode. Flow is from right to left.

The impact of the ionic wind on a 1 m/s bulk flow was found to be significant. As shown in Fig. 5, the flow was accelerated away from the centerline and impinged on the walls of the wind tunnel. At a greater corona current (40 μA), the ionic wind velocity became comparable to the bulk flow, and vorticial structures were formed at four locations near the electrodes – two sets of symmetric vortices across the centerline. The vortices appear typical of those due to an impinging flow, and the first set appears upstream of the collector electrode. These vortices generally caused the flow near the wall to significantly slow down upstream of the electrodes, including some flow reversal, and adversely affected convection. The second set of vortices appears between the two elec-

trodes, and it was near these vortices that the bulk flow was directed towards the walls and thus results in increased cooling. Of note is the position of the vortices relative to the wind tunnel walls. In an impinging flow in a static environment, two wall jets of equal magnitude are formed resulting in symmetric vortices across the impingement axis. However, that is not the case here. The upstream set of vortices was formed very close to the walls, similar to a wall jet. On the other hand, the second, downstream set was further from the wall, approximately halfway between the walls and the centerline. The presence of the bulk flow requires mass conservation, and therefore the downstream wall jet had a much faster speed than the upstream (reversed) wall jet. This accelerated wall jet pushed the downstream vortices away from the wall. Additionally, the downstream vortices were influenced by the flow entrained into the counter-flow ionic wind near the collecting electrode, which also pulled them away from the wall.

A different phenomenon was observed at the lower current of 20 μA. The flow was again redirected towards the wall, but does not behave like an impinging flow. There were no upstream vortices, and only smaller downstream vortices existed, due primarily to entrainment by the counter-flow ionic wind. In general, the redirection of the flow caused it to accelerate along the wall, enhancing convection. As the flow impinged on the wall, it was redirected towards the tunnel centerline. At the centerline, these redirected flows met slightly downstream of the electrodes and joined, continuing with comparable velocity to that of the bulk velocity upstream of the electrodes. The velocity was slightly reduced (from the bulk velocity value) along the centerline while it was slightly increased closer to the wall boundaries. This effect downstream of the electrodes appeared to subside with distance from the electrodes, though it was not measured directly.

When the bulk velocity was increased to 1.6 m/s, however, the effect of the ionic wind was much different (Fig. 6). The ionic wind was insufficient to effectively divert the flow toward the wall. However, it created a region of very low flow in the region of the collecting electrodes – essentially a flow blockage. Because of the mass conservation, this flow blockage caused the bulk flow to accelerate the reduced flow areas between the electrodes and walls. Thus, there was a noticeable acceleration of the flow, increasing by as much 0.5 m/s (~30 %). At a greater corona current (40 μA), the "blockage" was more effective so the wall acceleration was slightly greater, but not significantly so. These two cases were similar to the 20 μA/1.0 m/s flow in Fig. 5, but not comparable to the 40 μA/1.0 m/s flow. From all these measurements, there appears to be a critical matching of the ionic wind flow speed and the bulk speed. When the inertia of the bulk speed dominates, wall acceleration is the primary result, but when the inertia of the ionic wind dominates, an impinging flow is generated.

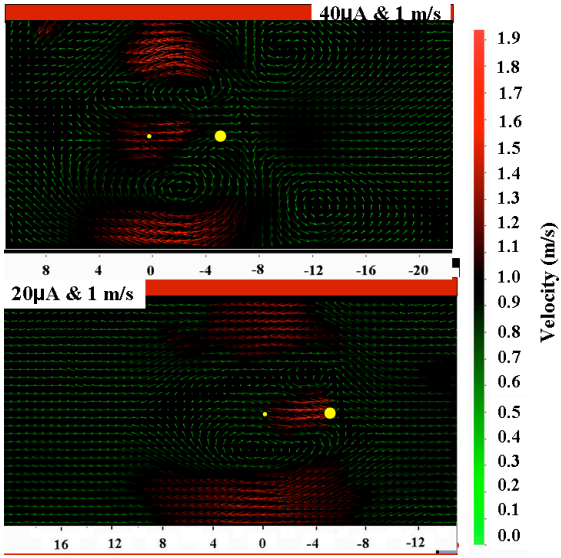


Fig. 5. PIV images for the case of 1 m/s bulk velocity and two corona currents, 20 μA and 40 μA. The larger yellow dot indicates the collecting electrode, and the smaller yellow dot indicates the corona electrode. The bulk flow is from right to left. Distance scales in mm are attached to each plot for reference.

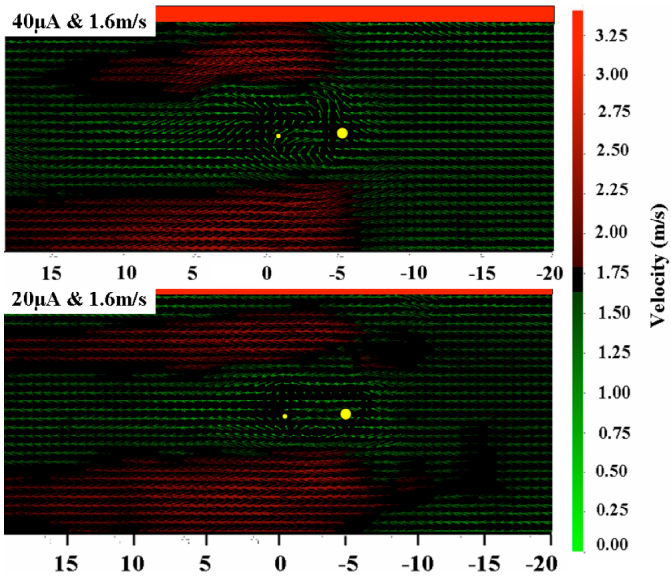


Fig. 6. PIV images for the case of 1.6 m/s bulk velocity and two corona currents, 20 μA and 40 μA. The larger yellow dot indicates the collecting electrode, and the smaller yellow dot indicates the corona electrode. The bulk flow is from right to left. Distance scales in mm are attached to each plot for reference.

### *B. Heat transfer*

For all the cases considered, the ionic wind increased the heat transfer at the location of the thermocouples, causing the steady state wall temperature to drop as shown in Fig. 7.

For all cases, the enhancement begins upstream of the electrodes at thermocouple 1 (11 mm upstream of the corona wire) and increases in the flow direction. However, though not directly measured due to the position of the thermocouples, at some downstream position the effect of the enhancement will diminish. The largest temperature decrease, and thus greatest heat transfer enhancement, was observed for the combination of 40 μA current and 1 m/s bulk flow velocity. The other three cases (20 μA/1.0 m/s, 40 μA/1.6 m/s, 20 μA/1.6 m/s) all had a similar smaller effect. These results correlate well with the PIV measurements. Recall that the film heaters extended 31 mm upstream of the electrodes such that the flow experienced heating prior to meeting the counter-flow ionic wind (and locations of the thermocouples). For the three cases of 20 μA/1.0 m/s, 40 μA/1.6 m/s, and 20 μA/1.6 m/s, the counter-flow ionic winds caused the flow to accelerate along the heated wall, increasing the advection and a corresponding increase in heat transfer. A 30 % increase in wall flow speed corresponds to a 30 % increase in $\mathrm{Re}_L$. As the Nusselt number goes with the square root of Reynolds number for external flow ($Nu_L \propto \mathrm{Re}_L^{1/2}$), which this flow approximates, only a 14 % increase in heat transfer coefficient is anticipated, accounting for the modest temperature reductions. However, for 40 μA ionic wind and 1 m/s bulk flow velocity, the impinging flow actually drew colder flow from the centerline towards the wall, a phenomenologically different enhancement mechanism where the nature of the flow was fundamentally changed. The impingement of colder air resulted in the greatest heat transfer enhancement in this study. From a design perspective, as noted in the PIV results, this suggests that one of the most important factors in maximizing heat transfer enhancement is generating a counter-flow ionic wind that can overcome the inertia of the bulk to generate an impinging flow.

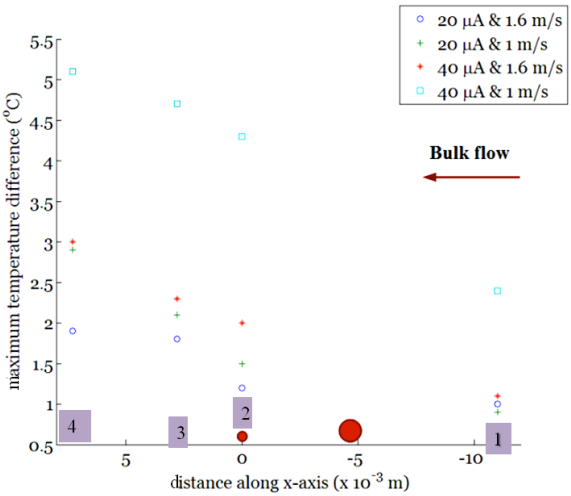


Fig. 7. Steady state temperature reduction due to counter-flow ionic wind as a function of location corresponding to the four thermocouple locations as noted in the numbered boxes. The larger red dot indicates the collecting electrode, and the smaller red dot indicates the corona electrode, whose center was located at x = 0.

## IV. PARTICLE MODELING

### *A. Purpose*

PIV requires the introduction of a seeding particle into the fluid flow for measurement purposes, and the measurement assumes these seeding particles follow the fluid motion. However, as the particles pass through a corona discharge, they could become charged, and Coulombic forces due to the electric field may cause the seeding particles to deviate from the bulk fluid flow, skewing the PIV measurements. Attempts have been made by some researchers to optimize seeding particles for use in PIV in non-thermal plasma discharges [18]. Another study reported the usage of PIV to study flow velocities in an electrostatic precipitator (ESP) model [19], reporting that the seeding particles were affected by the charges and the electric field. In order to have confidence in the fidelity of these PIV results, a model of the influence of charging and the electric field on seeding particles was constructed. To simplify the modeling, a co-flow scenario was assumed, but the results suggest that the counter-flow configuration in the experiments does not behave appreciably differently.

### *B. Governing Equations and Boundary Conditions*

To simulate the motion of a charged particle, the equation of motion was derived from the modified Basset-Boussinesq-Oseen (BBO) equation [20]. The BBO equation describes the general (linear) equation of motion for a small spherical particle suspended in a fluid.

$$\frac{\pi}{6}d_p^3\rho_p\frac{dU_p}{dt} = -3\pi\mu d(U_p - U) + \frac{\pi d_p^3}{6}\rho_f\frac{dU}{dt} - \frac{1}{2}\frac{\pi d_p^3}{6}\rho_f\frac{d(U_p - U)}{dt} + \sum_i F_i, \qquad (1)$$

where $d_p$ is the diameter of the particle (m), $\rho_p$ is the mass density of the particle (kg/m$^3$), $U_p$ is the particle velocity (m/s), $t$ is time (s), $\mu$ is dynamic viscosity (N-s/m$^2$), $U$ is fluid velocity (m/s), $\rho_f$ is the fluid density (kg/m$^3$), and $F_i$ denotes other external forces. The terms on the right hand side (RHS) are forces due to Stokes drag, pressure gradient, added mass, and other external forces respectively. This equation was modified to take into account the Coulombic force that results due to the presence of charges and electric field. Dielectrophoretic forces, which arise from permittivity gradients, were not taken into consideration as the permittivity variation was neglected, and for the same reason, the electrostrictive force was also not taken into account. Therefore the equation of motion in $x$-direction becomes

$$\frac{\pi}{6}d_p^3\rho_p\frac{dU_{p,x}}{dt} = -3\pi\mu d(U_{p,x} - U_x) + \frac{\pi d_p^3}{6}\rho_f\frac{dU_x}{dt} - \frac{1}{2}\frac{\pi d_p^3}{6}\rho_f\frac{d(U_{p,x} - U_x)}{dt} + E_x ne. \qquad (2)$$

Similarly, in the $y$-direction normal to the tunnel walls, it becomes of the form

$$\frac{\pi}{6}d_p^3\rho_p\frac{dU_{p,x}}{dt} = -3\pi\mu d U_{p,y} - \frac{1}{2}\frac{\pi d_p^3}{6}\rho_f\frac{dU_{p,y}}{dt} + E_y ne, \tag{3}$$

where $n$ is the number of charges on the particle, $e$ is elementary charge ($=1.6\times10^{-19}$ C), $E$ is the electric field (V/m), and subscripts $p$, $x$, and $y$ denote particle, $x$-direction and $y$-direction respectively. For these simulations, the bulk fluid was assumed to have a zero velocity in the $y$-direction so that terms having bulk velocity dropped out of the equation of motion in the $y$-direction. The gravity term was found to be negligible compared to the other terms and was neglected for this simulation.

These two equations were solved for the $x$ and $y$ velocity and subsequent $x$ and $y$ positions as a function of time through direct integration. The initial condition for the particle speed was assumed to be the bulk velocity in the $x$-direction only. Since the electric field and corona-generated ions are primarily confined to the region between the electrodes, it was assumed that the seeding particle does not get charged until it has reached the location of the electrodes. The initial location of the particle was aligned with the corona wire, and the motion was tracked until the particle had passed the collecting electrode where the electric field becomes negligible.

The critical force in the two BBO equations is the Coulombic force due to the electric field, and this was determined using the multiphysics modeling and engineering simulation software COMSOL. Poisson's equation was solved to determine the electric potential $V$,

$$\nabla^2 V = -\frac{q}{\varepsilon_0}, \tag{4}$$

where $q$ is space charge density (C/m$^3$) due to positive ions in the electrode gap, $\varepsilon_0$ is the dielectric permittivity of free space (= 8.854 x $10^{-12}$ F/m), and $E$ is related to the electric potential by

$$\vec{E} = -\vec{\nabla}V, \tag{5}$$

The space charge in the gap was modeled using the steady state ion transport equation

$$\vec{\nabla}.\vec{j} = 0, \tag{6}$$

where the current $j$ is

$$\vec{j} = \mu_E \vec{E} q - D\vec{\nabla}q. \tag{7}$$

The terms on the RHS represent the contribution to current due to electric drift and diffusion, respectively, where $\mu_E$ is the ion mobility ($2\times10^{-4}$ m$^2$ V$^{-1}$s$^{-1}$) and $D$ is the diffusion coefficient of ions (m$^2$ s$^{-1}$). Note that advection is much smaller than drift [21] and has

been neglected. The ionization zone is limited to a very narrow radius near the corona electrode and is negligible for the purpose of simulation.

The domain used for simulation corresponded to the length and width of that of the tunnel. At the inlet, outlet, and walls, a homogenous Neumann condition was used for Poisson's equation and Dirichlet conditions were used on the two electrodes. For the ion transport equation, Kaptsov's assumption and Peek's critical electric field were employed. Kaptsov's assumption states that the electric field in the ionization region near the corona electrode remains constant once the corona onsets, regardless of the applied potential, and Peek solved the critical electric field for corona onset. A Dirichlet boundary condition for the charge density $q$ at the corona electrode region was adjusted such that the electric field at the electrode surface, when solved self-consistently from Poisson's equation, matched the critical field determined by Peek. Current density was assumed to be zero at the wall boundaries and at the inlet and outlet (homogeneous Dirichlet), and a homogenous Neumann condition was assumed for the collecting electrode [22]. This is valid as the diffusion term in the current equation is negligible compared to the drift term [23].

### *C. Charging Mechanisms*

To accurately predict the Coulombic force in the BBO equations, (Eq. 2 and 3), the number of charges $n$ on the particle is required. Particle charging can occur by many mechanisms such as attachment of ions and static electrification. In this problem, ion attachment was presumed to be the dominant charging mechanism [24], and two modes of ion attachment are possible – diffusion charging and field charging. Diffusion charging becomes prominent for particles < 0.1 μm in diameter, even if an electric field is present. For seeding particles generated from smoke, the majority of the particles will be about an order of magnitude greater than this value [25] such that diffusion charging is negligible. Field charging occurs due to the electric field in the medium. If the permittivity of the particle is higher than that of the medium surrounding it, the field lines will converge towards it, and ions will travel along these field lines toward the particle. Thus field charging is the result of directed ion-particle collisions, and it is the primary charging mechanism for particle diameters > 0.4 μm when at least a moderate field is present. Hence in this simulation only field charging was considered. Field charging was modeled using Pauthenier theory [26], which states that given sufficient time for charging, a spherical particle will reach a maximum total charge, $p_{max}$ (C), known as the Pauthenier limit, and it is directly proportional to the electric field,

$$p_{\max} = 4\pi\varepsilon_0 a^2 E \frac{3\varepsilon_p}{\varepsilon_p + 2\varepsilon_0}, \tag{8}$$

where $\varepsilon_p$ is the dielectric permittivity of the particle (F/m) and $a$ is the radius of the particle (m). The amount of charge $p$ (C) acquired by the spherical particle during an exposure to an ion density of $N$ for a time $t$ is

$$p = p_{\max} \frac{t}{t + 4\varepsilon_0 / e\mu_E N}. \tag{9}$$

The amount of charge $p = ne$ was determined using Eqs. (8) and (9) for each time step $t$ in the integration of Eqs. (2) and (3) based on the local electric field calculated by Eq. (5).

### *D. Results*

For these studies, a potential of 5000 V was applied at the corona electrode and the collecting electrode was at ground. The electrode separation was 5 mm, and the bulk fluid velocity was set at 2 m/s. The seeding particle size was assumed to be 1 μm and the density was assumed to be 1100 kg/m$^3$. Charging was found to be prominent only in positions very near the corona electrode where the field was very high, on the order of $10^6$ to $10^7$ V/m in this study. As this is a corona discharge, the field rapidly decreases towards the collector electrode, where the field was of the order of $10^3$ V/m. Hence the charging rate reduced significantly as the particle moved away from the corona electrode. From Fig. 8., the maximum number of charges acquired by the seeding particle was ~15 over 3.5 ms, which corresponds to a distance of ~7 mm covering the electrode separation. This maximum number of charges was for a seeding particle whose initial position was in the vicinity of the electrode plane. For a seeding particle whose position was further away from the electrode plane, the field charging would negligible because the electric field was significantly smaller in those regions. The corresponding deviation of the particle velocity from that of the bulk fluid was found to be minimal in both the $x$ and $y$ directions (Fig. 9). The initial jump in deviation is because the particle starts with the same velocity as that of the fluid. Hence there is no drag force to oppose the Coulombic force in the initial time steps. Since the initial particle location was in the vicinity of the high field corona region, the deviation is larger than that expected for a counter-flow case. Additionally, the majority of seeding particles do not pass close to the corona electrode where the electric field is highest. For a seeding particle with the worst case of $n = 15$ charges and a velocity of 2 m/s at a location where field value is $10^5$ V/m as is the case in the majority of the electrode gap, the drag force/Coulombic force ratio is ~1500, suggesting minimal impact on the particle tracking the flow. Hence the influence of the corona discharge environment should have negligible influence on the majority of the seeding particles for these PIV studies.

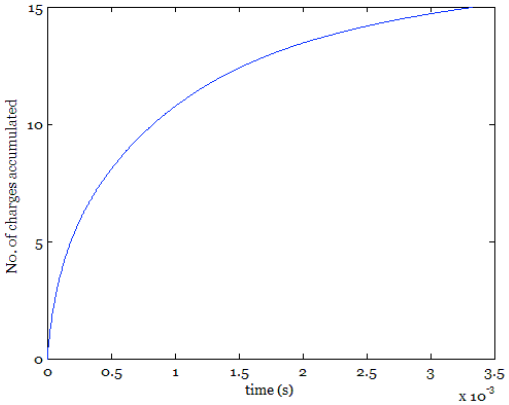


Fig. 8. Charge accumulation on a seeding particle in a corona discharge environment as a function of time for an initial position immediately adjacent to the corona electrode.

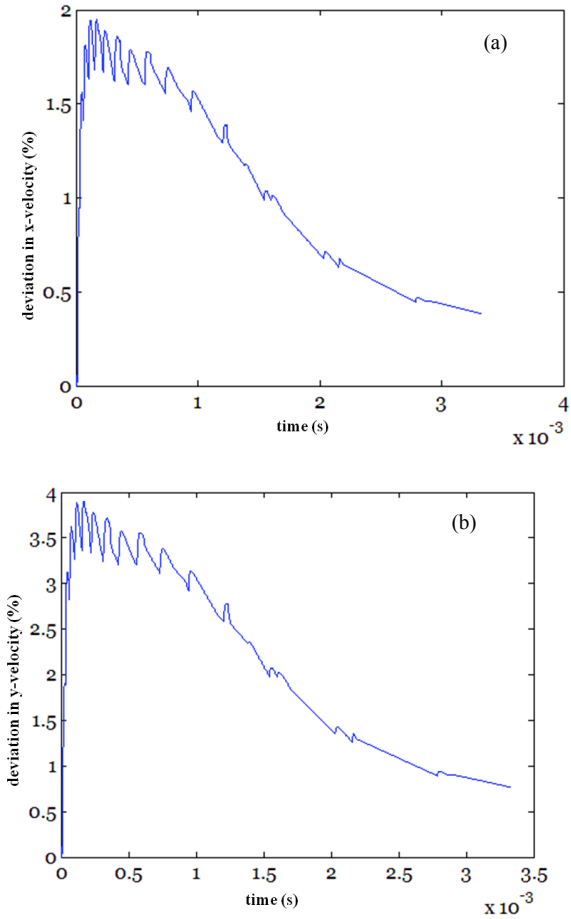


Fig. 9. Percentage deviation of the particle velocity from that of the bulk fluid as a function of time in the (a) *x*-direction and (b) *y*-direction.

## V. Conclusion

In this work, a counter-flow ionic wind was applied to enhance heat transfer from a heated plate undergoing a bulk flow. Particle image velocity and heat transfer measurements showed that the enhancement is maximized when the inertia of the counter-flow ionic wind overcomes that of the bulk flow, resulting in an impinging flow drawing cooler fluid directly to the plate surface. While the enhancement measured here was not significantly large, the enhancement can be improved and optimized by refining the electrode arrangement and operating conditions, using the current results as a guide. Modeling of seeding particles in the corona discharge environment showed that they are not significantly influenced by corona charging, giving confidence to the validity of the particle image velocity results.

## REFERENCES


[1] S.M. Marco and H.R. Velkoff, "Effect of electrostatic fields on free convection heat transfer," *ASME* Paper No. 63-HT-9, 1963.

[2] H. R. Velkoff and R. Godfrey, "Low-velocity heat transfer to a flat plate in the presence of a corona discharge in air," *J. Heat Transfer,* vol. 101, pp. 157-163, 1979.

[3] H. R. Velkoff, "Electrofluidmechanics: investigation of the effects of electrostatic fields on heat transfer and boundary layers," Aeronautical systems division, Air force systems command Wright-Patterson AFB, OH, ASD-TDR-62-650, 1962.

[4] D. B. Go, R. A. Maturana, T. S. Fisher, and S. V. Garimella, "Enhancement of external forced convection by ionic wind," *Int. J. Heat Mass Transfer*, vol. 51, pp. 6047-6053, 2008.

[5] D. B. Go, S. V. Garimella, T. S. Fisher and R. K. Mongia, "Ionic winds for locally enhanced cooling," *J. Appl. Phys*., vol. 102, no. 5, art. no. 053302, 2007.

[6] D. M. Bushnell, "Turbulent drag reduction for external flows," presented at AIAA 21st Aerospaces sciences meeting, Reno, NV, Jan. 1983, Paper AIAA-83-0227.

[7] M. R. Malik, L. M. Weinstein, and M. Y. Hussaini, "Ion wind drag reduction," presented at AIAA 21st Aerospace sciences meeting, Reno, NV, Jan. 1983, Paper AIAA-83-0231.

[8] S. El-Khabiry and G. M. Colver, "Drag reduction by dc corona discharge along an electrically conductive flat plate for small Reynolds number flow", *Phys. Fluids*, vol. 9, no. 3, pp.587-599, 1997.

[9] L. Léger, E. Moreau, and G. Touchard, "Control of low velocity airflow along a flat plate with a dc electrical discharge", *IEEE Trans. Ind. App*l. 38, 1478–1485, 2002.

[10] G. Artana, J. D'Adamo, L. Léger, E. Moreau, and G. Touchard, "Flow control with electrohydrodynamic actuators," *AIAA J.* , vol. 40, pp 1773–1779, 2002.

[11] E. Moreau, "Air control by non-thermal plasma actuators," *J.Phys. D: Appl. Phys*., vol. 40, no.3, pp. 605-636, 2007.

[12] G. M. Colver and Y. Nakai, "Flame stabilization by an electrical discharge and flame visualization of the influence of a semi-insulating wall on the ionic wind," in Proc. 13th IEEE-IAS annu. Meeting, Toronto, Ont., Ca., pp. 95-104, 1978.

[13] M. Molki, K .L. Bhamidipati, "Enhancement of convective heat transfer in the developing region of circular tubes using corona wind," *Int. J. Heat Mass Transfer*, vol. 47, pp. 4301-4314, 2004.

[14] P. H. G. Allen and T. G. Karayiannis, "Electrohydrodynamic enhancement of heat transfer and fluid flow," *Heat Reco. Systems & CHP*, vol. 15, No. 5, pp. 389-423, 1995.

[15] M. M. Ohadi, J. Darabi, and B. Roget, "Electrode design, fabrication, and materials science for EHD-enhanced heat and mass transport," *Ann. Rev. Heat Transfer*, vol. XI, pp. 563-632, 2001.

[16] S. Laohalertdecha, P. Naphon, and S. Wongwises, "A review of electrohydrodynamic enhancement of heat transfer," *Renewable & Susta. Energy Reviews*, vol. 11, no.5, pp. 858-876, 2007.

[17] NASA, Data on the emissivity of a variety of black paints, Available: http://masterweb.jpl.nasa.gov/reference/paints.htm

[18] J. S. Chang, D. Brocilo, K. Urashima, J. Mizeraczyk, J. Dekowski, J. Podlinski, M. Dors, M. Kocik, T. Ohkubo, S. Kanazawa, and Y. Nomoto, "Optimization of seed-particle size and density used in Particle Image Velocimetry under corona discharges and non-thermal plasmas," presented at 7th Int. Congress on Optical Particle Characterization, Kyoto, Japan, pp. 32-37, 2004.

[19] J. Mizeraczyk, J. Dekowski, J. Podliński, M. Kocik, T. Ohkubo, and S. Kanazawa, "Laser Flow Visualization and Velocity Fields by Particle Image Velocimetry in Electrostatic Precipitator Model," *J. Visualization*, vol. 6, no. 2, pp. 125-133, 2003.

[20] L. Fan, C. Zhu, *Principles of gas-solid flows*. 1st ed., Cambridge: Cambridge University Press, 1998, pp. 87–129.

[21] T. Yamamoto and H. R. Velkoff, " Electrohydrodynamics in electrostatic precipitator," *J. Fluid Mech*., vol. 108, pp. 1 - 18, 1981.

[22] S. Karpov and I. Krichtafovitch, "Electrohydrodynamic flow modeling using FEMLAB," presented at COMSOL multiphysics user's conference, Boston, MA, 2005.

[23] J. Q. Feng, "Electrohydrodynamic flow associated with unipolar charge current due to corona discharge from a wire enclosed in a rectangular shield," *J. Appl.Phy.*, vol. 86, no. 5, pp. 2412-2418, 1999.

[24] S. K. Friedlander, *Smoke,dust and haze: Fundamentals of aerosol dynamics.* 2nd ed., USA: Oxford University Press, 2000, pp. 40-50.

[25] S. W. See, R. Balasubramanian, and U.M. Joshi, "Physical characteristics of nanoparticles emitted from incense smoke," *Sci. technol. adv. Mater*., vol. 8, pp. 25-32, 2007.

[26] A. G. Bailey, *Electrostatic spraying of liquids.* Somerset, UK: Research Studies, 1988, pp. 35–39.